
First detection of methyl formate in the hot molecular core IRAS 18566+0408

Arijit Manna¹ • Sabyasachi Pal¹

Abstract The studies of the complex molecular emission lines in millimeter and submillimeter wavelengths towards the hot molecular cores demonstrate valuable details about the chemical complexity in the interstellar medium (ISM). We presented the first detection of the rotational emission lines of the complex organic molecule methyl formate (CH₃OCHO) towards the hot molecular core region IRAS 18566+0408 using the high-resolution Atacama Large Millimeter/Submillimeter Array (ALMA) band 3 observation. The estimated column density of CH₃OCHO using the rotational diagram analysis was $(4.1 \pm 0.1) \times 10^{15} \text{ cm}^{-2}$ with rotational temperature $102.8 \pm 1.2 \text{ K}$. The estimated fractional abundance of CH₃OCHO towards the IRAS 18566+0408 relative to hydrogen (H₂) was 3.90×10^{-9} . We noted that the estimated fractional abundance of CH₃OCHO is fairly consistent with the simulation value predicted by the three-phase warm-up model from Garrod (2013). We also discussed the possible formation mechanism of CH₃OCHO towards the hot molecular cores.

Keywords ISM: individual objects (IRAS 18566+0408) – ISM: abundances – ISM: kinematics and dynamics – stars: formation – astrochemistry

1 Introduction

The study of the hot molecular cores (HMCs), specially in the initial evolution phases, is difficult due to large distances ($\geq 1 \text{ kpc}$), complex cluster environments, and short evolution timescales ($\leq 10^4 \text{ years}$) (Silva et al. 2017). The HMCs are one of the early stages of star-formation, and

they play an important role in the ISM's chemical complexity (Shimonishi et al. 2021). The HMCs are mainly characterised by their small source size ($\leq 0.1 \text{ pc}$), high temperature ($\geq 100 \text{ K}$), and high density ($n_{\text{H}_2} \geq 10^7 \text{ cm}^{-3}$) (van Dishoeck & Blake 1998). The HMC regions contain high-velocity H₂O masers that are located near Ultra-Compact (UC) H II regions (Mehringer et al. 2004). The HMCs are the most chemically rich phase in the ISM and are characterised by the presence of complex organic molecules like methyl cyanide (CH₃CN), methyl isocyanate (CH₃NCO), methyl formate (CH₃OCHO), methanethiol (CH₃SH), dimethyl ether (CH₃OCH₃), methanol (CH₃OH), ethyl cyanide (C₂H₅CN), vinyl cyanide (C₂H₃CN), methylamine (CH₃NH₂), methylene imine (CH₂NH), aminoacetonitrile (NH₂CH₂CN), and cyanamide (NH₂CN) etc (Silva et al. 2017; Beuther et al. 2002; Shimonishi et al. 2021; Hofner et al. 2017; Gorai et al. 2021; Ohishi et al. 2019; Manna & Pal 2022a,b). The phase of HMCs is thought to last about $\sim 10^5 \text{ years}$ to $\sim 10^6 \text{ years}$ (van Dishoeck & Blake 1998; Garrod & Herbst 2006; Silva et al. 2017). The observations of the molecular lines in millimeter and submillimeter wavelengths with higher angular resolution were essential in understanding the chemical composition and physical properties molecular outflows of the HMCs (Silva et al. 2017).

The HMC candidate IRAS 18566+0408 (alternatively, G37.55+0.20) was located at a distance of 6.7 kpc (Sridharan et al. 2002). The far-infrared luminosity of IRAS 18566+0408 was $\sim 8 \times 10^4 L_{\odot}$, which originated from a single compact ($\geq 5''$) dust continuum source (Silva et al. 2017). The single compact dust continuum emission towards IRAS 18566+0408 indicated the presence of an O8 ZAMS high-mass star (Zhang et al. 2007; Sridharan et al. 2002; Silva et al. 2017). Earlier, Carral et al. (1999) and Araya et al. (2005) detected the first weak radio continuum emission from IRAS 18566+0408 at wavelengths of 2 cm and 3.6 cm with a very low flux density $\sim 0.7 \text{ mJy}$, which indicated that this source is in the initial stage of the development of the UC H II re-

Arijit Manna

Sabyasachi Pal

¹Midnapore City College, Kuturia, Bhadutala, Paschim Medinipur, West Bengal, India

email: arjitmanna@mcconline.org.in

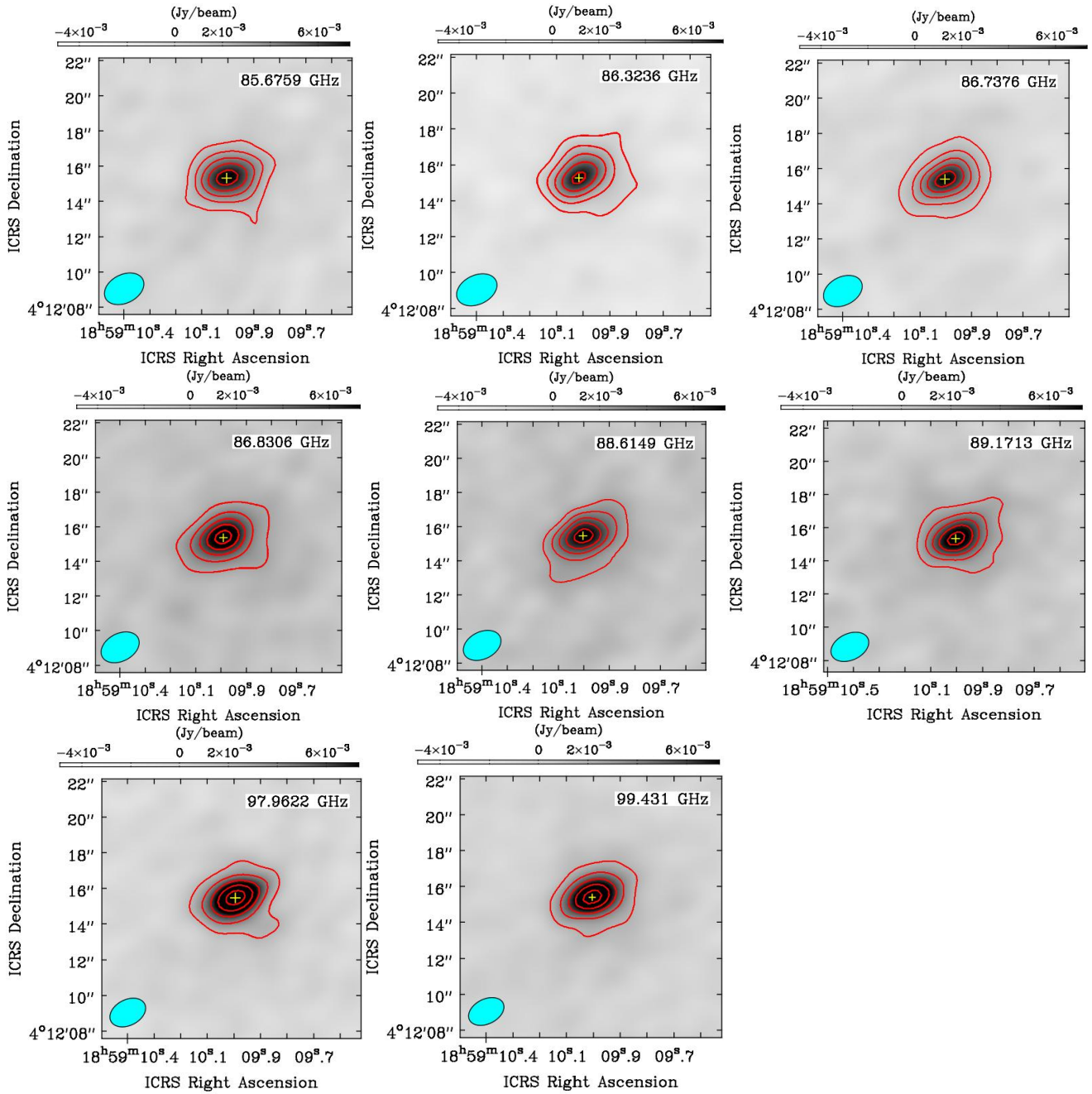


Fig. 1 Continuum images of IRAS 18566+0408 obtained with ALMA at frequency (i) 85.6759 GHz ($\sigma = 34.91 \mu\text{Jy beam}^{-1}$), (ii) 86.3236 GHz ($\sigma = 43.31 \mu\text{Jy beam}^{-1}$), (iii) 86.7376 GHz ($\sigma = 40.20 \mu\text{Jy beam}^{-1}$), (iv) 86.8306 GHz ($\sigma = 40.75 \mu\text{Jy beam}^{-1}$), (v) 88.6148 GHz ($\sigma = 31.93 \mu\text{Jy beam}^{-1}$), (vi) 89.1716 GHz ($\sigma = 47.30 \mu\text{Jy beam}^{-1}$), (vii) 97.9621 GHz ($\sigma = 45.39 \mu\text{Jy beam}^{-1}$), and (viii) 99.4310 GHz ($\sigma = 28.99 \mu\text{Jy beam}^{-1}$). The contour level started at 3σ , where σ is the RMS of each continuum images and contour level increased by a factor of $\sqrt{2}$. The cyan circles indicated the synthesized beam of the continuum images. The corresponding synthesized beam size of all continuum images were presented in Table. 1. The yellow cross-hair in the center of each continuum map indicated the peak continuum position.

gion. Recently, Hofner et al. (2017) detected the radio continuum emission from IRAS 18566+0408, which was resolved into 1.3 cm and 6 cm wavelengths, and they claimed that the radio continuum emission is consistent with an ionized jet. The HMC object IRAS 18566+0408 was classified as a massive disk candidate (Zhang 2005). The emission lines of maser methanol (CH_3OH) and water (H_2O) at frequencies of 6.7 GHz and 22 GHz were strongly evident towards IRAS 18566+0408 (Beuther et al. 2002). The emission lines of maser formaldehyde (H_2CO) at wavelength 6 cm were found from the IRAS 18566+0408 (Araya et al. 2005). The emission lines of ammonia (NH_3) with transitions $J = 1, 1$ and $J = 2, 2$ were detected by the single-dish radio telescopes towards IRAS 18566+0408 (Miralles et al. 1994; Molinari et al. 1996; Sridharan et al. 2002) and later Zhang et al. (2007) studied details of the emitting region of NH_3 towards IRAS 18566+0408 using the VLA. Recently, the molecular emission lines of methyl cyanide (CH_3CN), methanol (CH_3OH), carbonyl sulfide (OCS), carbon monoxide (^{12}CO , and ^{13}CO), sulfur monoxide (SO), and ethyl cyanide ($\text{C}_2\text{H}_5\text{CN}$) were detected towards IRAS 18566+0408 using the Submillimeter Array (SMA) but author does not discuss the formation mechanism of the detected molecules (Silva et al. 2017). A bipolar molecular outflow was evident towards IRAS 18566+0408, which was associated with a massive disk (Silva et al. 2017).

In the ISM, the complex organic molecule methyl formate (CH_3OCHO) was one of the most abundant organic molecular species, which was specially found in both high-mass and low-mass star formation regions (Brown et al. 1975; Cazaux et al. 2003). The emission lines of CH_3OCHO were first detected towards the Sgr B2(N) (Brown et al. 1975). Earlier, many chemical models indicated that the CH_3OCHO molecule was formed after the evaporation of the methanol (CH_3OH) from the grain mantle towards HMCs (Millar et al. 1991). Garrod et al. (2008) presented the formation mechanism of CH_3OCHO in gas-grain interaction, but how to produce CH_3OCHO in the ISM using gas-phase reactions is not well understood. The emission lines of CH_3OCHO also detected towards another HMC candidate G31.41+0.31 with an estimated column density $3.4 \times 10^{18} \text{ cm}^{-2}$ (Isokoski et al. 2013). The emission lines of CH_3OCHO were also seen in the low mass protostar IRAS 16293–2422 (Cazaux et al. 2003). The emission lines of methyl formate were also observed in the solar-type star-forming region L1157-B1, where the molecular outflow interacts with dense clouds (Arce et al. 2008). Earlier, Sakai et al. (2006) detected the emission lines of CH_3OCHO from NGC 1333 IRAS 4B, and the author claimed these molecules can be used as a tracer of complex biomolecules in the HMC regions. Therefore, CH_3OCHO was an important molecule on the grain surfaces of hot corinos and HMCs.

In this article, we presented the first detections of the rotational emission lines of CH_3OCHO towards IRAS 18566+0408 using ALMA band 3. This paper is organized as follows. In Section 2, we discussed the observations and data reductions. The result of the detection of CH_3OCHO was shown in Section 3. The discussion and summary were presented in Section 4 and 5.

2 Observations and data reduction

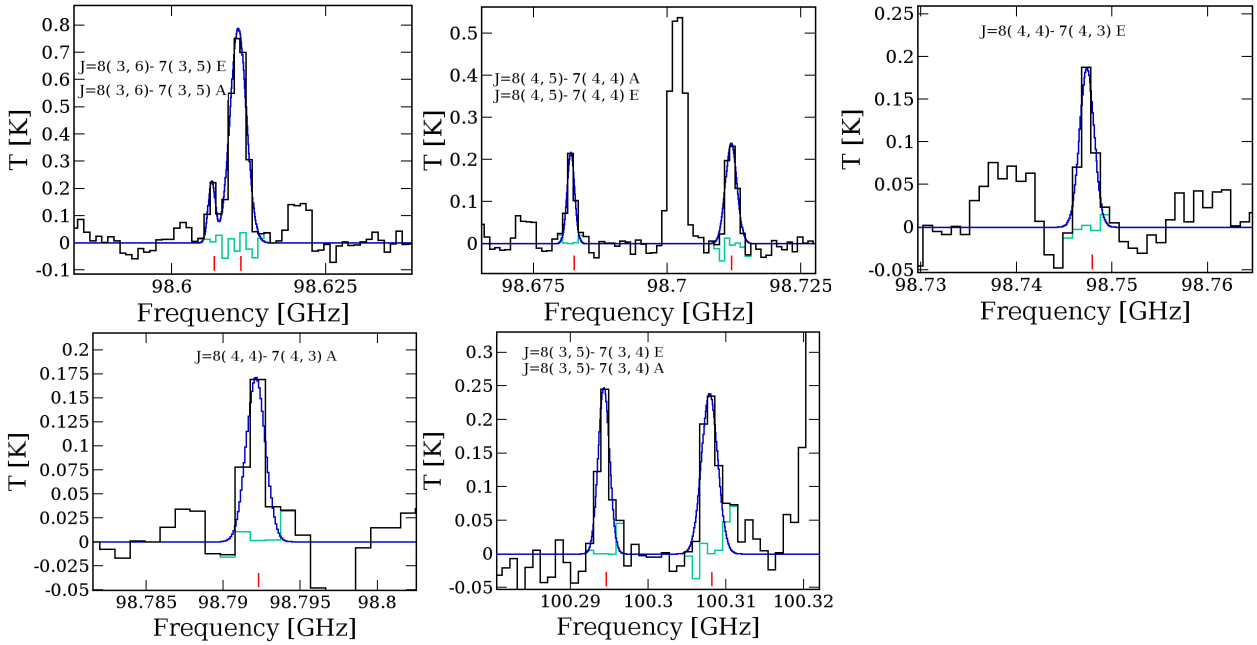
The millimeter-wavelength observation of HMC candidate IRAS 18566+0408 was performed with the Atacama Large Millimeter/Submillimeter Array (ALMA) using the band 3 (frequency range 85.64–100.42 GHz) receiver. The observed phase center of IRAS 18566+0408 was α_{J2000} : 18:59:10.000 and δ_{J2000} : +04:12:16.000. During the observation, XX, YY, and XY-type signal correlators were used via the integration times of 1360.800 Sec. The observations were done on 24-March-2016 with a minimum baseline of 41 m and a maximum baseline of 216 m. During the observation, a total of thirty-six antennas were used to study the molecular lines from IRAS 18566+0408. The solar planet Neptune was taken as a flux calibrator, J1924–2914 was taken as a bandpass calibrator, and J1830+0619 was taken as a phase calibrator. The systematic velocity (V_{LSR}) of IRAS 18566+0408 was $\sim 84.5 \text{ km s}^{-1}$ (Silva et al. 2017).

We used the Common Astronomy Software Application (CASA 5.4.1)¹ for initial data reduction and spectral imaging with the standard ALMA data reduction pipeline (McMullin et al. 2007). The continuum flux density of the flux calibrator Neptune for each baseline was scaled and matched with the Butler-JPL-Horizons 2012 flux calibrator model with 5% accuracy using task SETJY (Butler 2012). Initially, we calibrated the bandpass and flux by flagging the bad data using the CASA pipeline with task `hifa_flagdata` and `hifa_bandpassflag`. After the initial data reduction, we split the target data using task MSTRANSFORM with rest frequency in each spectral window. We used the task UVCONTSUB for the continuum subtraction procedure from the UV plane. After the continuum subtraction, we made the spectral image of IRAS 18566+0408 using task TCLEAN with the rest frequency of each spectral window. After the creation of the spectral data cube, we used the task IMPBCOR for the correction of the primary beam pattern in the synthesized image.

¹<https://casa.nrao.edu/>

Table 1 Summary of the continuum images of IRAS 18566+0408.

Frequency (GHz)	Integrated flux (mJy)	Peak flux (mJy beam ⁻¹)	Beam size ("×")	Position angle (°)	RMS (μJy beam ⁻¹)
85.6759	13.53±0.66	7.16±0.24	2.399×1.622	-64.029	34.91
86.3236	11.49±0.94	6.58±0.36	2.382×1.618	-64.527	43.31
86.7376	10.47±0.53	6.40±0.22	2.377×1.603	-64.119	40.20
86.8305	13.01±0.89	7.74±0.35	2.386×1.601	-64.750	40.75
88.6148	12.19±0.94	6.81±0.35	2.336×1.588	-64.442	31.93
89.1716	10.68±0.52	7.19±0.23	2.323×1.578	-64.442	47.30
97.9621	17.02±1.10	10.14±0.45	2.131×1.442	-64.997	45.39
99.4310	16.81±0.99	9.43±0.38	2.099×1.377	-64.329	28.99

**Fig. 2** Rotational emission lines of CH₃OCHO between the frequency range of 85.64–100.42 GHz with their different transitions towards IRAS 18566+0408. The continuum emission has been completely subtracted from the emission spectrum. The black line represented the observed emission spectra of CH₃OCHO, while the blue line presented a Gaussian profile fitted to the observed spectra. The green line indicated the residual of the spectra.**Table 2** Summary of the line parameters of CH₃OCHO towards IRAS 18566+0408

Species	Frequency [GHz]	Transition [$J''_{k''_a k''_c} - J''_{k''_a k''_c}$]	E_u [K]	A_{ij} [s ⁻¹]	Peak intensity [K]	$S\mu^2$ [Debye ²]	FWHM [km s ⁻¹]	V_{LSR} [km s ⁻¹]	$\int T_{mb} dv$ [K km s ⁻¹]	Remark
CH ₃ OCHO	98.6069	8(3,6)–7(3,5)E	27.26	1.20×10^{-5}	0.211	18.246	5.230±0.31	84.50±0.25	1.287±0.32	Non blended
CH ₃ OCHO	98.6112	8(3,6)–7(3,5)A	27.24	1.20×10^{-5}	0.748	18.273	7.665±0.69	84.15±0.31	7.334±0.96	Blended with C ₂ H ₅ CN
CH ₃ OCHO	98.6826	8(4,5)–7(4,4)A	31.89	1.05×10^{-5}	0.212	15.966	7.658±1.23	84.21±0.55	1.358±0.29	Blended with NCCONH ₂
CH ₃ OCHO	98.7120	8(4,5)–7(4,4)E	31.90	1.02×10^{-5}	0.227	15.436	7.628±0.75	84.38±0.92	1.256±0.39	Blended with NCCONH ₂
CH ₃ OCHO	98.7479	8(4,4)–7(4,3)E	31.91	1.02×10^{-5}	0.187	15.440	6.682±0.98	84.18±0.86	1.287±0.21	Non blended
CH ₃ OCHO	98.7923	8(4,4)–7(4,3)A	31.89	1.05×10^{-5}	0.171	15.963	7.289±1.28	84.26±0.68	2.361±0.82	Non blended
CH ₃ OCHO	100.2946	8(3,5)–7(3,4)E	27.41	1.26×10^{-5}	0.245	18.259	6.289±0.98	84.30±0.86	8.172±1.83	Non blended
CH ₃ OCHO	100.3082	8(3,5)–7(3,4)A	27.40	1.26×10^{-5}	0.239	18.283	6.325±0.82	84.31±0.96	8.372±1.98	Non blended

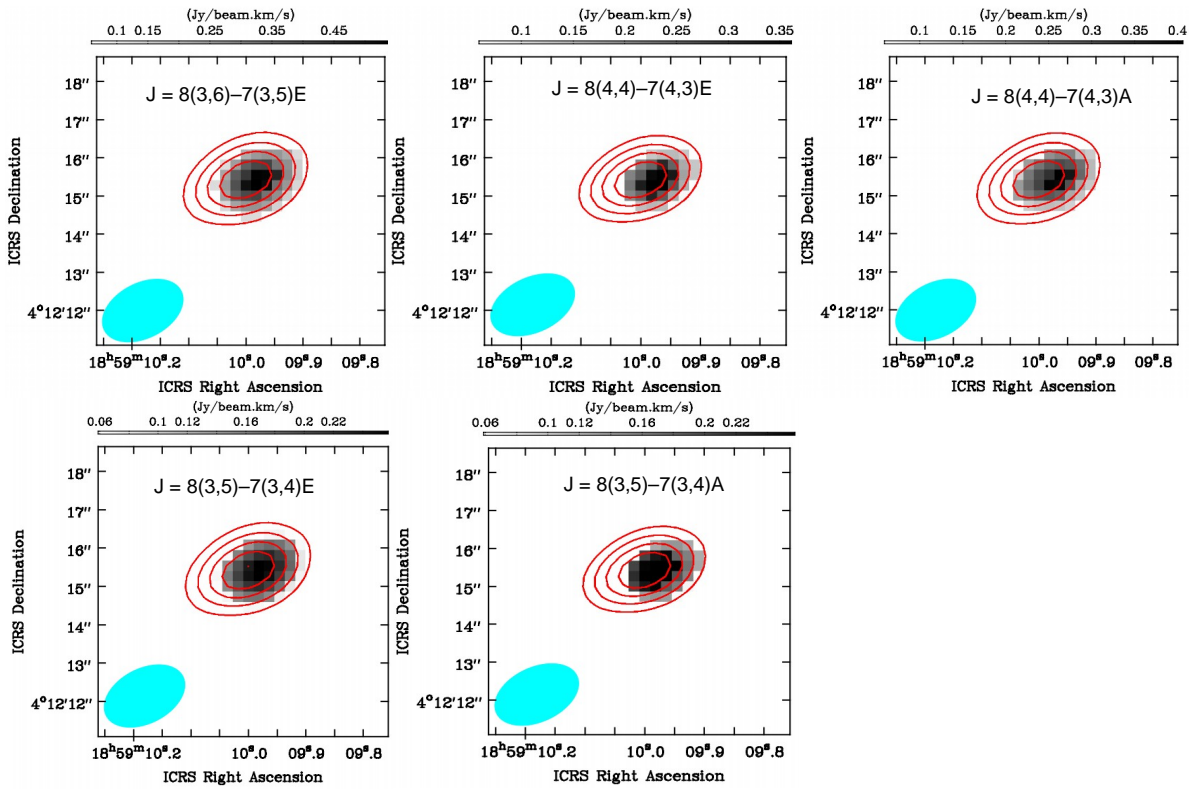


Fig. 3 Integrated emission map of unblended transitions of CH_3OCHO , which are overlaid with 3.015 mm of continuum emission (red contour). The contour levels are at 20%, 40%, 60%, and 80% of the peak flux. The cyan circles indicate the synthesized beam of the integrated emission map.

3 Results

3.1 Continuum emission towards IRAS 18566+0408

We presented the millimeter continuum emission towards IRAS 18566+0408 at frequencies of 85.6759 GHz (3.499 mm), 86.3236 GHz (3.472 mm), 86.7376 GHz (3.456 mm), 86.8305 GHz (3.452 mm), 88.6148 GHz (3.383 mm), 89.1716 GHz (3.361 mm), 97.9621 GHz (3.060 mm), and 99.4310 GHz (3.015 mm), which is presented in Figure 1, where the surface brightness colour scale has the unit of Jy beam⁻¹. After generating the continuum emission map, we used CASA task IMFIT to fit the 2D Gaussian over the continuum image and obtained an integrated flux density, peak flux density, synthesized beam size, position angle, and RMS, which is presented in Table. 1. We observed that the continuum image was larger than the synthesized beam size for each images, which indicated the continuum emission was resolved between the observable frequency ranges.

3.2 Estimation of hydrogen (H₂) column density and optical depth (τ_ν) towards IRAS 18566+0408

For optically thin dust continuum emission, the flux density (S_ν) can be expressed as,

$$S_\nu = \tau_\nu B_\nu(T_d) \Omega_{beam} \quad (1)$$

where, τ_ν indicated the optical depth, T_d is dust temperature, $B_\nu(T_d)$ presented the Planck function at dust temperature T_d (Whittet 1992), and $\Omega_{beam} = (\pi/4 \ln 2) \times \theta_{major} \times \theta_{minor}$ was the solid angle of the synthesized beam. The equation of optical depth can be written as,

$$\tau_\nu = \rho_d \kappa_\nu L \quad (2)$$

where, ρ_d presented the mass density of dust, κ_ν was the mass absorption coefficient, and L indicated the path length. The mass density of the dust can be expressed as in terms of the dust-to-gas mass ratio (Z),

$$\rho_d = Z \mu_H \rho_{H_2} = Z \mu_H N_{H_2} 2m_H / L \quad (3)$$

Table 3 Column density of hydrogen and optical depth.

Wavelength (mm)	Hydrogen column density (cm ⁻²)	Optical depth (τ_ν)
3.499	1.18×10^{24}	0.00495
3.472	1.05×10^{24}	0.00457
3.456	1.01×10^{24}	0.00445
3.452	1.21×10^{24}	0.00538
3.383	9.64×10^{23}	0.00473
3.361	1.01×10^{24}	0.00501
3.060	1.06×10^{24}	0.00702
3.015	9.42×10^{23}	0.00656
Average Value	1.05×10^{24}	0.00533

where, μ_H indicated the mean atomic mass per hydrogen, ρ_{H_2} is the mass density of hydrogen, m_H is the mass of hydrogen, and N_{H_2} is the column density of hydrogen. We used dust temperature $T_d = 170$ K (Hofner et al. 2017), $\mu_H = 1.41$, and $Z = 0.01$ (Cox & Pilachowski 2000). The estimated peak flux density of the dust continuum of the IRAS 18566+0408 at different frequencies are presented in Table. 1. From equations 1, 2, and 3, the column density of molecular hydrogen can be expressed as,

$$N_{H_2} = \frac{S_\nu / \Omega}{2\kappa_\nu B_\nu(T_d) Z \mu_H m_H} \quad (4)$$

During the estimation of the mass absorption coefficient (κ_ν), we adopted the formula $\kappa_\nu = 0.90(\nu/230\text{GHz})^\beta \text{ cm}^2 \text{ g}^{-1}$ (Motogi et al. 2019), where $k_{230} = 0.90 \text{ cm}^2 \text{ g}^{-1}$ indicated the emissivity of the dust grains at a gas density of 10^6 cm^{-3} , which covered by a thin ice mantle at 230 GHz. We used the dust spectral index $\beta \sim 1.3$ (Zhang et al. 2007; Silva et al. 2017). Using the adopted mass absorption coefficient formula, we obtained the value κ_ν is 0.249, 0.251, 0.253, 0.254, 0.260, 0.262, 0.296, and 0.302 for the frequencies 85.6759 GHz, 86.3236 GHz, 86.7376 GHz, 86.8305 GHz, 88.6148 GHz, 89.1716 GHz, 97.9621 GHz, and 99.4310 GHz respectively. We estimated the column density of hydrogen for the eight frequency regions towards IRAS 18566+0408 which was presented in Table. 3. We take the average value to determine the resultant hydrogen column density towards IRAS 18566+0408. The obtained column density of hydrogen towards IRAS 18566+0408 was $\sim 1.05 \times 10^{24} \text{ cm}^{-2}$, which was estimated taking the average of these eight continuum values. After the estimation of the hydrogen column density, we also estimated the value of optical depth (τ_ν) using the following equation,

$$T_{mb} = T_d(1 - \exp(-\tau_\nu)) \quad (5)$$

where, T_{mb} indicated the brightness temperature and T_d is the dust temperature of IRAS 18566+0408. During the estimation of the brightness temperature, we used the Rayleigh-Jeans approximation, $1 \text{ Jy beam}^{-1} \equiv 118 \text{ K}$. The estimated dust optical depth of eight individual frequency regions was presented in Table. 3. The average dust optical depth is estimated to be 0.00533. The estimated dust optical depth indicated that the HMC candidate IRAS 18566+0408 is optically thin between the frequency range 85.64–100.42 GHz.

3.3 Line emission towards IRAS 18566+0408

We extracted the millimeter spectra of IRAS 18566+0408 to create a 2.5'' diameter circular region centred at RA (J2000) = (18^h59^m09^s.92), Dec (J2000) = (4°12'15".58). After

the extraction of the millimeter spectra, we used the CASSIS² (Vastel et al. 2015) for the identification of the molecular emission lines towards IRAS 18566+0408 using the Cologne Database for Molecular Spectroscopy (CDMS)³ (Müller et al. 2005) or Jet Propulsion Laboratory (JPL)⁴ (Pickett et al. 1998) spectroscopic molecular databases. After the spectral analysis, we detected rotational emission lines of CH₃OCHO towards the IRAS 18566+0408 between the frequency ranges of 85.64–100.42 GHz with spectral resolution 1128.91 kHz. We identified a total of eight strong rotational transition lines of CH₃OCHO towards IRAS 18566+0408. There were no missing transition lines of CH₃OCHO within the observed frequency range.

After the identification of emission lines of CH₃OCHO from the millimeter spectra of IRAS 18566+0408, we fitted the Gaussian model over the observed spectra of CH₃OCHO using the line analysis module in CASSIS. We estimated the Full-Width Half Maximum (FWHM), quantum numbers ($J'_{K'_a K'_c} - J''_{K''_a K''_c}$), upper state energy (E_u), Einstein coefficients (A_{ij}), peak intensity and integrated intensity ($\int T_{mb} dV$) after fitting a Gaussian model over the observed spectra of CH₃OCHO. The summary of the detected transitions of CH₃OCHO and Gaussian fitting parameters of CH₃OCHO was presented in Table 2 and the observed spectra of CH₃OCHO with Gaussian fitting were shown in Figure 2. In the case of CH₃OCHO, the torsional substates are noticed due to the internal rotation of the methyl group. So, we observed the A and E sub-states of CH₃OCHO. We carefully checked for the possible line contamination in the spectral profiles of CH₃OCHO with nearby molecular transitions during the spectral analysis using the line analysis module in CASSIS. We observed $J = 8(3,6) - 7(3,5)A$, $J = 8(4,5) - 7(4,4)A$, and $J = 8(4,5) - 7(4,4)E$ transition lines of CH₃OCHO blended with C₂H₅CN and NCCONH₂ respectively. We observed that the $J = 8(4,4) - 7(4,3)A$ transition line of CH₃OCHO does not have a proper Gaussian shape due to lower spectral resolution, but this transition is not blended with other nearby molecular transitions.

3.4 Spatial distribution of CH₃OCHO towards IRAS 18566+0408

We created the integrated emission map of CH₃OCHO using the task IMMOMENTS in CASA. The integrated emission maps were created by integrating the spectral data cubes in the velocity range where the emission lines of CH₃OCHO were detected. We created the emission map only for the unblended transition lines of CH₃OCHO. The integrated emission map was shown in Figure 3, which was overlaid on

the 3.015 mm continuum emission. The resultant emission map indicated that the emission lines of CH₃OCHO arise from the warm inner region of IRAS 18566+0408. We also observed that the lines of CH₃OCHO have a peak at the position of the continuum. After the generation of the emission map, we fitted a 2D Gaussian over the integrated map using CASA task IMFIT. The deconvolved beam size of the emitting region was calculated from the following equation

$$\theta_S = \sqrt{\theta_{50}^2 - \theta_{beam}^2} \quad (6)$$

where $\theta_{50}^2 = 2\sqrt{A}/\pi$ indicated the diameter of the circle whose area was enclosing 50% line peak and θ_{beam} indicated the half-power width of the synthesized beam (Manna & Pal 2022a,b). The estimated emitting region of unblended transitions of CH₃OCHO is presented in Table 4. The emitting region of CH₃OCHO varies between 1.120''–1.213''. We noticed that the emitting region of CH₃OCHO is smaller than the synthesized beam size, which indicates all transitions of CH₃OCHO were not spatially resolved.

3.5 Rotational diagram analysis

We have detected the multiple hyperfine transitions of CH₃OCHO with different upper-state energy (E_u). So, we used the rotational diagram method to obtain the column density (N) in cm⁻² and rotational temperature (T_{rot}) in K of detected emission lines of CH₃OCHO towards IRAS 18566+0408. We used the rotational diagram method because we assumed that the observed species were optically thin and that they were populated in Local Thermal Equilibrium (LTE) conditions. The assumption of Local Thermodynamic Equilibrium condition was reasonable towards the IRAS 18566+0408 due to very high densities (2.6×10^7 cm⁻³ in the inner regions of hot core (Silva et al. 2017)). The column density of optically thin emission lines can be expressed as (Goldsmith & Langer 1999),

$$N_u^{thin} = \frac{3g_u k_B \int T_{mb} dV}{8\pi^3 \nu S \mu^2} \quad (7)$$

Table 4 Estimated emitting regions of CH₃OCHO towards IRAS 18566+0408.

Molecule	Transition [$J'_{K'_a K'_c} - J''_{K''_a K''_c}$]	Emitting region [']
CH ₃ OCHO	8(3,6)–7(3,5)E	1.129
	8(4,4)–7(4,3)E	1.120
	8(4,4)–7(4,3)A	1.213
	8(3,5)–7(3,4)E	1.135
	8(3,5)–7(3,4)A	1.133

²<http://cassis.irap.omp.eu/?page=cassis>

³<https://cdms.astro.uni-koeln.de/cgi-bin/cdmssearch>

⁴<https://spec.jpl.nasa.gov/>

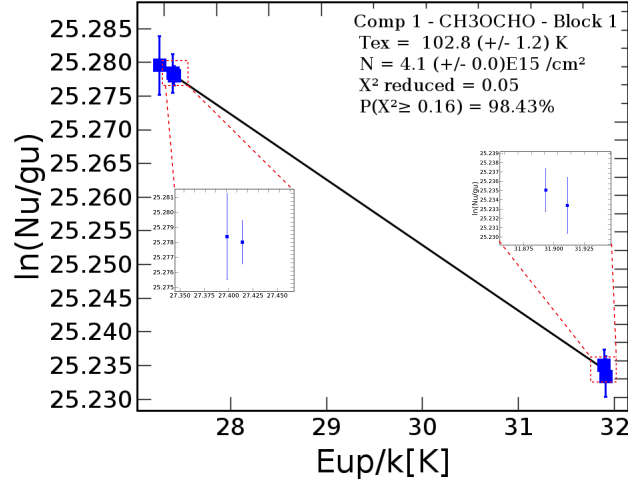


Fig. 4 Rotational diagram of CH₃OCHO towards IRAS 18566+0408. The blue blocks indicated the statistical data points and the solid black lines presented the fitted straight lines which estimated the column density and rotational temperature. The vertical blue error bars were the absolute uncertainty of $\ln(N_u/g_u)$.

where, g_u presented the degeneracy of the upper state energy (E_u), k_B is the Boltzmann constant, $\int T_{mb}dV$ indicated the integrated intensity of the detected emission lines, μ is the electric dipole moment, S is the strength of the transition lines, and ν is the rest frequency of observed molecules. Under the LTE conditions, the column density of the detected molecules can be expressed as,

$$\frac{N_u^{thin}}{g_u} = \frac{N_{total}}{Z(T_{rot})} \exp(-E_u/k_B T_{rot}) \quad (8)$$

where, T_{rot} is the rotational temperature, $Z(T_{rot})$ is the partition function at extracted rotational temperature, and E_u is the upper state energy of the observed molecules. The equation 8 can be rearranged as,

$$\ln\left(\frac{N_u^{thin}}{g_u}\right) = \ln(N) - \ln(Z) - \left(\frac{E_u}{k_B T_{rot}}\right) \quad (9)$$

Equation 9 demonstrated the linear relationship between the E_u and $\ln(N_u/g_u)$. The column density and rotational temperature can be estimated by fitting a straight line to the values of $\ln(N_u/g_u)$ which is plotted as a function of E_u . The value of N_u/g_u is estimated from equation 7. For the rotational diagram analysis, we extracted the line parameters like FWHM, upper state energy (E_u), line intensity, and integrated intensity ($\int T_{mb}dV$) using a Gaussian fitting over the observed spectra of CH₃OCHO which presented in Table 2. During the rotational diagram analysis, we used only unblended transitions of the detected species. The computed rotational diagram of CH₃OCHO was shown in Figure 4. In the rotational diagram, the vertical blue error bars were the absolute uncertainty of $\ln(N_u/g_u)$, and it was generated from the error of the observed $\int T_{mb}dV$, which was

measured using the fitting of Gaussian model over observed transitions of CH₃OCHO. Using the rotational diagram analysis, we found the column density of CH₃OCHO was $(4.1 \pm 0.1) \times 10^{15} \text{ cm}^{-2}$ with rotational temperature 102.8 ± 1.2 K. Our estimated rotational temperatures of CH₃OCHO are similar to the typical hot core temperature because of the temperature of hot core above 100 K (Gorai et al. 2021). After the estimation of the column density, we estimated the fractional abundance of CH₃OCHO which was 3.90×10^{-9} . The fractional abundance of CH₃OCHO were estimated with respect to H₂, where column density of H₂ towards IRAS 18566+0408 was $1.05 \times 10^{24} \text{ cm}^{-2}$ (see Section. 3.2).

4 Discussion

4.1 comparison between observed and simulation abundance of CH₃OCHO

Here, we presented a comparison between observational results and existing astrochemical simulations of CH₃OCHO. We followed the three-phase warm-up model of Garrod (2013) to compare the observational and simulation results. Garrod (2013) considered an isothermal collapse phase, which is followed by a static warm-up phase. In the first phase, the number density increases from $n_H = 3 \times 10^3$ to 10^7 cm^{-3} under the free-fall collapse, and the dust temperature is reduced to 8 K from 16 K. In the second phase, the density remains fixed at $\sim 10^7 \text{ cm}^{-3}$ where the dust temperature fluctuates from 8 K to 400 K. The temperature of IRAS 18566+0408 was ~ 170 K, which is a typical hot core temperature, and the number density (n_H) of this source is $2.6 \times 10^7 \text{ cm}^{-3}$ (Hofner et al. 2017; Silva et al.

Table 5 Comparison between simulated and observed fractional abundance of CH₃OCHO

Species	Simulated Values ^a						Observed Values ^b	
	Fast		Medium		Slow		IRAS 18566+0408	
	Abundance	T (K)	Abundance	T (K)	Abundance	T (K)	Abundance	T (K)
CH ₃ OCHO	9.2×10^{-8}	120	3.7×10^{-8}	111	3.1×10^{-9}	103	3.90×10^{-9}	102.8

Notes: a – Values taken from Table 8 of [Garrod \(2013\)](#);

b – this work.

2017). Thus, the hot core model of [Garrod \(2013\)](#) is suitable for understanding the chemical evolution towards the IRAS 18566+0408. [Garrod \(2013\)](#) used the fast, medium, and slow warm-up models based on the time scale. The time scale of the fast warm-up model is more suitable for studying the chemical evolution of HMC regions ([Gorai et al. 2021](#)). In Table 5, we compare the observed fractional abundance of CH₃OCHO with the simulated abundance results of [Garrod \(2013\)](#) and we noticed the slow warm-up model of [Garrod \(2013\)](#) satisfied our estimated abundance of CH₃OCHO towards IRAS 18566+0408. [Garrod \(2013\)](#) estimated that the abundance of CH₃OCHO towards the HMCs environment is 3.1×10^{-9} with temperature 103 K under the slow warm-up conditions and we estimated the abundance of CH₃OCHO towards HMC object IRAS 18566+0408 was 3.90×10^{-9} with temperature 102.8 K, which indicated a good agreement between the simulation and observational results.

4.2 Possible formation mechanism of CH₃OCHO

Here, we discuss the possible formation mechanism of CH₃OCHO towards HMCs. In this article, we presented the first detection of CH₃OCHO towards IRAS 18566+0408 using the ALMA. In ISM, CH₃OCHO molecule can efficiently be created on the surface of dust grains by the reaction between CH₃O and HCO, and this mechanism is the same for the case of all HMCs ([Garrod et al. 2008](#); [Garrod 2013](#)). The chemical simulation between CH₃O and HCO shows that these radicals are mobile around 30–40 K and the reaction is efficient ([Gorai et al. 2021](#)). According to the simulation of Figure 1 in [Garrod \(2013\)](#), it is clear that the gas phase CH₃OCHO in the HMC region mainly comes from the ice phase. The increasing of UV photodissociation of CH₃OH in the HMCs leads to the formation of CH₂O, CH₃O, and CH₃ around 40 K temperature, and these are mobile and create complex organic molecules, e.g., CH₃OCHO, CH₃OCH₃ ([Gorai et al. 2021](#)). At temperature $T \sim 40$ K in gas phase, the H₂CO and protonated CH₃OH (when it is abundantly released to the gas phase) react and create H₅C₂O₂⁺ ([Gorai et al. 2021](#)). The CH₃OCHO would be created in the HMCs via the electron recombination of H₅C₂O₂⁺ (H₅C₂O₂⁺+e⁻ → CH₃OCHO+H) ([Bonfand et](#)

[al. 2019](#)). Earlier, [Balucani et al. \(2015\)](#) proposed an efficient gas-phase reaction of CH₃OCHO in the cold environment where CH₃OCH₃ was behaving as a possible precursor of CH₃OCHO. Recently, [Silva et al. \(2017\)](#) detected the single transition line of CH₃OCH₃ with transition J = 17(2,15)–16(3,14) towards IRAS 18566+0408 using SMA but the detection of a single transition line of a complex molecule is not a strong enough conclusive evidence of the presence of the molecule in HMCs. Therefore, CH₃OCHO can be produced through both grain surface and gas-phase reactions in the ISM.

5 Summary

In this article, we presented the detection of complex biomolecule CH₃OCHO at millimeter wavelengths towards the HMC candidate IRAS 18566+0408 using the ALMA. The main results are as follows.

- We reported the first detection of the rotational emission lines of CH₃OCHO towards the HMC region IRAS 18566+0408 using ALMA band 3 between the frequency range of 85.64–100.42 GHz.
- From the dust continuum emission, the estimated column density of hydrogen (H₂) was 1.05×10^{24} cm⁻². We also estimated that the dust optical depth was 0.00533, which indicated IRAS 18566+0408 is optically thin between the frequency range of 85.64–100.42 GHz.
- The estimated column density of CH₃OCHO towards IRAS 18566+0408 was $(4.1 \pm 0.1) \times 10^{15}$ cm⁻² with rotational temperature 102.8 ± 1.2 K. We also estimated the fractional abundance of CH₃OCHO towards IRAS 18566+0408 with respect to H₂ is 3.90×10^{-9} . Our estimated rotational temperature indicated that the emission line of CH₃OCHO arises from the warm inner region of IRAS 18566+0408 because the temperature of the hot core, in general, is above 100 K.
- We compared our estimated abundance of CH₃OCHO with the three-phase warm-up model of [Garrod \(2013\)](#). After the comparison, we noticed that the slow warm-up model of [Garrod \(2013\)](#) satisfied the abundance of CH₃OCHO towards IRAS 18566+0408.
- After the successful detection of CH₃OCHO towards IRAS 18566+0408, a broader study was needed to search

other molecular lines in the other frequency bands of ALMA to understand the chemical complexity in this HMC.

Acknowledgments

The plots within this paper and other findings of this study are available from the corresponding author upon reasonable request. This paper makes use of the following ALMA data: ADS/JAO.ALMA#2015.1.00369.S. ALMA is a partnership of ESO (representing its member states), NSF (USA), and NINS (Japan), together with NRC (Canada), MOST and ASIAA (Taiwan), and KASI (Republic of Korea), in cooperation with the Republic of Chile. The Joint ALMA Observatory is operated by ESO, AUI/NRAO, and NAOJ.

Data availability

The data that support the plots within this paper and other findings of this study are available from the corresponding author upon reasonable request. The raw ALMA data are publicly available at <https://almascience.nao.ac.jp/asax/> (project id: 2015.1.00369.S).

Funding

No funds or grants were received during the preparation of this manuscript.

Conflicts of interest

The authors declare no conflict of interest.

Author Contributions

A.M analysis the ALMA data and identify the emission lines of methyl formate from IRAS 18566+0408. A.M and S.P wrote the main manuscript text. All authors reviewed the manuscript.

References

Araya, E., Hofner, P., Kurtz, S., et al. 2005, *ApJ*, 618, 339
 Arce, H. G., Santiago-Garcia, J., Jørgensen, J. K., et al. 2008, *ApJL*, 681, L21
 Balucani N., Ceccarelli C., Taquet V. 2015, *MNRAS*, 449, L16
 Butler B. 2012, ALMA Memo Series, NRAO

Bonfand, M., Belloche, A., Garrod, R.T., et al. 2019, *A&A*, 628, A27
 Brown, R.D., Crofts, J.G., Godfrey, P. D., et al. 1975, *ApJ*, 197, L29
 Beuther H., Schilke P., Sridharan T. K., et al. 2002, *A&A*, 383, 892
 Cazaux, S., Tielens, A. G. G. M., Ceccarelli, C., et al. 2003, *A&A*, 593, L51
 Carral, P., Kurtz, S., Rodriguez, L. F., et al. 1999, *RMxAA*, 35, 97
 Cox, A. N., & Pilachowski, C. A. 2000, *Physics Today*, 53, 77
 Garrod, R. T. & Herbst, E. 2006, *A&A*, 457, 927
 Garrod, R. T., Weaver, S. L. W., & Herbst, E. 2008, *ApJ*, 682, 283
 Garrod R. T. 2013, *ApJS*, 765, 60
 Goldsmith, P. F., & Langer, W. D. 1999, *ApJ*, 517, 209
 Gorai, P., Das, A., Shimonishi, T., et al. 2021, *ApJ*, 907, 108.
 Hofner P., Cesaroni R., Kurtz S., et al. 2017, *ApJ* 843 99
 Isokoski K., Bottinelli S., & van Dishoeck E. F. 2013, *A&A*, 554, A100
 Manna, A. & Pal, S., 2022, *Life Sciences in Space Research*, 34, 9
 Manna, A. & Pal, S., 2022, accepted in *Journal of Astrophysics and Astronomy*
 Mehringer, D. M., Pearson, J. C., Keene, J., & Phillips, T. G. 2004, *ApJ*, 608,306-313
 Motogi, K., Hirota, T., Machida, M. N., et al. 2019, *ApJL*, 877, L25
 Molinari S., Brand J., Cesaroni R., & Palla, F., 1996, *A&A*, 308, 573
 Miralles M. P., Rodriguez L. F., & Scalise, E. 1994, *ApJS*, 92, 173
 McMullin, J. P., Waters, B., Schiebel, D., et al. 2007, San Francisco, CA: ASP, 127
 Millar, T. J., Herbst, E., & Charnley, S. B. 1991, *ApJ*, 369, 147
 Müller, H. S. P., Schlmöder, F., Stutzki, J. & Winnewisser, G. 2005, *Journal of Molecular Structure*, 742, 215–227
 Ohishi, M., Suzuki, T., Hirota, T., Saito, M. & Kaifu, N. 2019, *PASJ*, 71
 Pickett, H. M., Poynter, R. L., Cohen, E. A., et al. 1998, *Journal of Quantitative Spectroscopy and Radiative Transfer*, 60, 883
 Silva A., Zhang Q., Sanhueza P., et al. 2017, *ApJ*, 847, 1538
 Sridharan T. K., Beuther H., Schilke P., et al. 2002, *ApJ*, 566, 931
 Shimonishi, T., Izumi, N., Furuya, K., & Yasui, C., 2021, *ApJ*, 2, 206
 Sakai, N., Sakai, T., Yamamoto, S. 2006, *PASJ*, 58, L15
 van Dishoeck E. F., & Blake G. A. 1998, *Annu Rev Astron Astrophys*, 36, 317
 Vastel, C., Bottinelli, S., Caux, E., et al. 2015, *Proceedings of the Annual meeting of the French Society of Astronomy and Astrophysics*, 313-316
 Whittet, D. C. B. 1992, *Journal of the British Astronomical Association*, 102, 230
 Zhang Q., 2005, in *Massive Star Birth: A Crossroads of Astrophysics*, ed. R. Cesaroni et al. (Cambridge: Cambridge Univ. Press), 135
 Zhang Q., Sridharan T. K., Hunter T. R., et al., 2007, *A&A*, 470, 269